Universal behavior of electron g -factors in semiconductor nanostructures

Athmane Tadjine, Yann-Michel Niquet, Christophe Delerue

Universal behavior of electron g-factors in semiconductor nanostructures

Athmane Tadjine,[1] Yann-Michel Niquet,[2,*] and Christophe Delerue[1,†]
[1]*Université Lille, CNRS, Centrale Lille, ISEN, Université Valenciennes, UMR 8520-IEMN, F-59000 Lille, France*
[2]*Université Grenoble Alpes, INAC-MEM, L_Sim, Grenoble, France*
and CEA, INAC-MEM, L_Sim, 38000 Grenoble, France
(Received 13 March 2017; revised manuscript received 7 June 2017; published 30 June 2017)

We combine analytic developments and numerical tight-binding calculations to study the evolution of the electron g-factors in homogeneous nanostructures of III-V and II-VI semiconductors. We demonstrate that the g-factor can be always written as a sum of bulk and surface terms. The bulk term, the dominant one, just depends on the energy gap of the nanostructure but is otherwise isotropic and independent of size, shape, and dimensionality. At the same time, the magnetic moment density at the origin of the bulk term is anisotropic and strongly dependents on the nanostructure shape. The physical origin of these seemingly contradictory findings is explained by the relation between the spin-orbit-induced currents and the spatial derivatives of the electron envelope wave function. The tight-binding calculations show that the g-factor versus energy gap for spherical nanocrystals can be used as a reference curve. In quantum wells, nanoplatelets, nanorods, and nanowires, the g-factor along the rotational symmetry axis can be predicted from the reference curve with a good accuracy. The g-factors along nonsymmetric axes exhibit more important deviations due to surface contributions but the energy gap remains the main quantity determining their evolution. The importance of surface-induced anisotropies of the g-factors is discussed.

DOI: 10.1103/PhysRevB.95.235437

I. INTRODUCTION

In the last decades, researchers have managed to synthesize nanostructures with a plethora of sizes, shapes, and compounds [1–6]. In particular, colloidal approaches enabled the synthesis of spherical nanocrystals, nanorods, nanowires, and nanoplatelets [7–9]. Promising applications for these nanocrystals have emerged such as solar cells, displays, photodetectors, and molecular sensing [10–16].

Among different techniques used to characterize these nanocrystals, those involving magnetic fields become increasingly important. Optical experiments under strong magnetic field enable the investigation of the excitonic fine structure [17–23]. Electron spin resonance through the measurement of g-factors is a remarkable tool to probe the electron (hole) states in nanocrystals in which the number of electrons is controlled by doping [24–27] or by the stoichoimetry [28]. Optically detected magnetic resonance reveals information about the spin multiplicity of band edge states and provides means to identify surface/interface sites [29].

These studies are also important because semiconductor nanostructures are good candidates for spintronic and quantum computing devices [30–33]. The spin can be manipulated by tuning the effective g-tensor using an applied electric field [31,34–36]. In this context, knowing the g-factor values is of crucial importance. However, the experimental measurement of the electron g-factor is not straightforward as, in many studies, only the exciton g-factor is obtained [17–23,37,38].

In the literature, theoretical works on electron g-factors are mainly limited to specific systems like quantum wells and spherical quantum dots [34,39–44]. The electron g-factor in spherical CdSe quantum dots has been calculated and measured. It is found that it strongly varies with size but there are discrepancies between the calculated values [19,21,42,43,45]. More generally, a clear picture of the behavior of the electron g-factor with nanocrystal size, shape, and dimensionality is still missing. It is also needed to go beyond the prototypical case of CdSe for nanocrystals. Our main aim in this paper is to provide such a picture for nanostructures of homogeneous composition belonging to the wide class of compounds characterized by a direct gap at Γ.

A first indication of a possible rationalization of the g-factors can be found in the theory of Kiselev *et al.* [40] based on the envelope function approximation and on the Kane $\mathbf{k}\cdot\mathbf{p}$ Hamiltonian [46,47], which accounts for the coupling of the conduction band to the top valence bands. The remote band contributions are included in a term Δg treated as a fitting parameter, which is expected to be small. Analytic expressions are derived for the g-factor in spherical quantum dots, nanowires, and quantum wells [44]. Interestingly, one can deduce from this theory a nontrivial result if Δg is neglected. The g-factor in quantum dots, nanowires, and quantum wells is given by the same expression (given below) when the nanostructures have an homogeneous composition and their surface essentially behaves as a hard wall for the electron (infinite barrier limit), i.e., in conditions usually realized in homogeneous colloidal nanocrystals.

A second indication of a rationalization of the g-factors is given by the work of Yugova *et al.* [48] showing that the out-of-plane g-factor in GaAs/$Al_xGa_{1-x}As$ quantum wells has a universal dependence on the lowest band-to-band optical transition energy, and this universality also embraces $Al_xGa_{1-x}As$ alloys.

Quite surprisingly, the fact that g-factors for systems of different dimensionalities could be given by the same expression has not received particular attention. In addition, if this fact is confirmed, its physical origin is far from trivial since recent works demonstrate that the orbital magnetic moment at

*yann-michel.niquet@cea.fr
†christophe.delerue@iemn.univ-lille1.fr

the origin of the deviation of g from g_0 comes from electrical currents induced by the spin-orbit coupling, and is strongly dependent on the size and the shape of a nanostructure [49,50]. Therefore the situation is confusing. It is thus needed to investigate the g-factors of nanocrystals with different shapes and to understand the physical origin of the orbital magnetic moment in a more general framework. It is also important to use more elaborate methodologies for the calculations, in particular, to include remote band contributions.

In this work, in a first step, we use an atomistic tight-binding approach to calculate the electron g-factor of homogeneous nanostructures, i.e., made from a single compound, namely, CdSe, CdTe, GaAs, InP, InAs, or InSb. In each case, several sizes and shapes are investigated. We show that the electron g-factor is mainly determined by the energy gap of the nanocrystals and happens to be almost shape-independent, especially for its component along a rotational symmetry axis. We discuss the importance of g-factor anisotropies and their sensitivity to the surface. In a second step, we use analytic developments to show that the g-factor can be decomposed into bulk and surface components. We investigate the physical reasons why the bulk term is independent of the size, shape, and dimensionality of the nanostructure, except through its energy gap. We explain why this isotropic and universal behavior is compatible with a magnetic moment density strongly dependent on the electron wave function [49,50].

The paper is organized as follows. The methodology of the tight-binding calculations is described in Sec. II. The results for bulk semiconductors and for spherical nanocrystals are presented in Secs. III and IV, respectively. The results for nanostructures with other shapes are given in Sec. V in which we investigate the universal behavior of the g-factors. The g-factor anisotropies are quantified and analyzed in Sec. VI. In Sec. VII, we propose an analytic expression for the g-factors. We use it to explain the origin of the universal behavior of the g-factors. The physical consequences of these findings are discussed.

II. METHODOLOGY

We have explored homogeneous nanostructures with different dimensionalities, shapes and sizes. We have calculated the g-factor in 3D (bulk), 2D (quantum wells), 1D (cylindrical and square nanorods/nanowires), and 0D (spheres, cubes, circular, and square nanoplatelets). By convention, the quantum wells (nanoplatelets) are confined along the z direction. The axis of the nanorods and nanowires is also taken along the z direction.

A. Tight-binding calculations

The atomistic tight-binding method is implemented as follows. The nanocrystals have a zinc-blende structure for which each atom is described by a double set of $sp^3d^5s^*$ atomic orbitals, including the spin degree of freedom. The spin-orbit coupling is included as intra-atomic Hamiltonian matrix elements in the p sector. The orbitals are assumed to be orthogonal and only nearest-neighbor couplings are considered. The tight-binding parameters are derived in Ref. [51] for CdSe, Ref. [52] for CdTe, Ref. [53] for GaAs, InP and InAs, and Ref. [54] for InSb.

In this work, we only investigate nanostructures with well passivated surfaces in such a way that the carriers are strongly confined in the semiconductor core. However, different passivations are conceivable since, experimentally, the surfaces can be covered with different types of ligands or capping layers (e.g., oxides). Therefore we have considered two models of passivation. In the first one, each dangling bond at the surface is saturated by a pseudo-hydrogen atom described in the tight-binding model by a single s orbital which is coupled to the s and p orbitals of the surface atoms. This is described in the tight-binding model by the following parameters: $E_H = 0$ eV for the on-site s orbital energy (the zero of energy corresponding to the top of the bulk valence band), and $V_{ss\sigma} = -3.5$ eV and $V_{sp\sigma} = 4.5$ eV for the hopping terms (notations of Ref. [55]). These values are sufficient to push the surface states out of the gap region, even in small nanocrystals.

In the second passivation model, we effectively remove from the basis of orbitals the sp^3 hybrid orbitals that form the dangling bonds at the surface. This second approach is close to the infinite barrier model commonly used to describe strongly confined carriers, for instance, in the envelope function approximation [56,57]. In contrast, the first model describes a smoother confinement potential.

For the sake of conciseness, the results presented in this paper are obtained using the first passivation model for GaAs, InP, and InAs, and using the second model for CdSe, CdTe, and InSb. The effects related to these different passivations will be discussed in Sec. VI.

We have also calculated the electron g-factors of GaAs/$Al_xGa_{1-x}As$ quantum wells (Sec. V D). The $Al_xGa_{1-x}As$ alloy is described as a virtual crystal defined by tight-binding parameters interpolated between GaAs and AlAs [53].

In Appendix A, we also present calculations of the g-factors in InSb quantum wells covered by a thin CdTe shell. In absence of lattice mismatch between InSb and CdTe, we have employed the same tight-binding parameters as for the homogeneous compounds in their respective regions. At the InSb/CdTe interface, the hopping terms are taken as simple averages over the two compounds. We assume a valence-band offset between InSb and CdTe of 0.87 eV [58].

B. g-factor calculations

The g-factors are deduced from two different approaches. The use of one rather than the other depends on the dimensionality of the system and on the system (Hamiltonian matrix) size. For small systems, both methods are feasible, we have checked that they give the same results.

1. Peierls phase approach

In this case, a weak magnetic field is included using Peierls substitution as derived in Ref. [59]. The g-factor is thus obtained from the splitting of the lowest conduction level of the nanocrystal. This approach was used to calculate the g-factor in all 0D systems (spherical quantum dots, nanoplatelets and nanorods). The calculations are feasible even for structures containing a large number of atoms (up to 4 millions) because they do not require the calculation of all the eigenstates of the Hamiltonian. A partial diagonalization approach as described in Ref. [60] is sufficient.

TABLE I. Bulk electron g-factor (g_{bulk}) at 0 K from experiments [Exp.] and tight-binding [TB] calculations. $\mathbf{k}\cdot\mathbf{p}$ parameters obtained in TB compared to literature values [Lit.]: E_g^b is the energy gap, Δ_{SO} is the spin-orbit energy, and E_p is the interband coupling matrix element in the Kane model [47]. $\tilde{g}_0$ and E_0 are the parameters of Eq. (4) determined from the fit of the g-factors of spherical nanocrystals vs the energy gap (reference curve).

Compound	g_{bulk} [TB]	g_{bulk} [Exp.]	E_g^b (eV)	Δ_{SO} (eV)	E_p (eV) [TB]	E_p (eV) [Lit.]	$\tilde{g}_0$	E_0 (eV)
CdSe	0.633	0.68 [66]	1.8174	0.3871	21.40	17.5 [67]	2.179	2.2247
CdTe	−1.236	−1.66 [68]	1.6108	0.8221	19.57	21.07 [69]	2.684	3.1172
GaAs	−0.065	−0.44 [70]	1.5190	0.3399	25.34	25.5−29.0 [71];25.61 [64]	2.673	2.4617
InP	1.224	1.20 [68]	1.4236	0.1077	20.45	20.93 [69];16.6–20.7 [71];18.74 [64]	2.195	1.3737
InAs	−14.20	−14.70 [72]	0.4176	0.3801	21.11	21.5–22.2 [71];21.30 [64]	2.590	1.6610
InSb	−62.68	−51.3 [73,74]	0.2253	0.8729	27.40	23.3 [71];24.34 [64]	0.685	1.7105

In 0D nanostructures, it is always possible to consider a sufficiently small magnetic field $\mathbf{B}$ in such a way that the Zeeman splitting is small compared to the distance in energy between the lowest conduction level and the other discrete levels. Therefore the g-factor can be also calculated using first-order perturbation theory in which the magnetic part of the Hamiltonian $-\boldsymbol{\mu}\cdot\mathbf{B} = \mu_B/\hbar(g_0\mathbf{s}+\mathbf{l})\cdot\mathbf{B}$ is treated as a small perturbation. Here, $\mu_B = e\hbar/(2m_0)$ is the Bohr magneton, $-e$, m_0 and $g_0 = 2.0023$ are the free-electron charge, mass, and g-factor, respectively. $\mathbf{s}$ and $\mathbf{l}$ are the spin and orbital momentum operators, respectively. The g-factor along z is then given by

$$g_z = g_0 + 2\langle\Psi_{c\uparrow}|l_z|\Psi_{c\uparrow}\rangle/\hbar, \tag{1}$$

where $\Psi_{c\uparrow}$ is the lowest conduction state of spin up calculated in the absence of a magnetic field [61]. Similar equations hold along x and y. In the absence of spin-orbit coupling, the wave function $\Psi_{c\uparrow}$ can be chosen purely real, the matrix elements of the imaginary operator $\mathbf{l}$ are necessarily equal to zero [62]. Therefore any deviation of g from g_0 is induced by the effect of the spin-orbit coupling on the electron wave function.

2. $\mathbf{k}\cdot\mathbf{p}$ *approach*

For extended systems (1D-2D-3D), another approach is often used to deduce the g-factor. This is in particular required when it is not possible to find a gauge that preserves the original periodicity of the Hamiltonian on the lattice [59]. The effective electron g-factor along z can be written as [63,64]

$$g_z = g_0 - 2\frac{i}{m_0}\sum_n \frac{\langle\Psi_{c\uparrow}|\hat{p}_x|\Psi_n\rangle\langle\Psi_n|\hat{p}_y|\Psi_{c\uparrow}\rangle}{E_c - E_n} - \frac{\langle\Psi_{c\uparrow}|\hat{p}_y|\Psi_n\rangle\langle\Psi_n|\hat{p}_x|\Psi_{c\uparrow}\rangle}{E_c - E_n}, \tag{2}$$

where n runs over all possible electronic states Ψ_n of energy E_n, E_c is the energy of the state $\Psi_{c\uparrow}$ of spin up along z. All states are calculated at $\mathbf{k} = 0$. The matrix elements of the momentum operator $\hat{\mathbf{p}}$ are deduced from those of the derivative of the tight-binding Hamiltonian with respect to the wave vector, as described in Ref. [59]. A full diagonalization of the Hamiltonian matrix is required in order to take into account the coupling with all electronic states Ψ_n. This limits the number of atoms per unit cell that can be treated using this approach to ≈1000. As expected, the main contributions to the sum in Eq. (2) come from the top valence band states. However, the contribution of the other states, especially conduction band states, is not negligible (Ref. [65]). For convenience, the numerical values of all data (approximately 370 energy gaps and 620 g-factors) presented in this paper are provided in Ref. [65].

III. BULK SEMICONDUCTORS

The electron g-factor (g_{bulk}) deviates from g_0 due to the action of the spin-orbit coupling (discussed in detail below) [40,63,70,75]. This gives various values of g_{bulk} for the different compounds (Table I), ranging from small deviations from g_0 such as in InP ($g_{\text{bulk}} = 1.224$) to large ones, for instance, in InSb ($g_{\text{bulk}} = -62.68$).

The calculated values are in rather good agreement with the data from the literature. To estimate the discrepancy between TB values and experiments, $|g_{\text{bulk}} - g_0|$ is the meaningful quantity, which is actually calculated. The error between the TB and experimental values of $|g_{\text{bulk}} - g_0|$ is of 18% for InSb, 15% for GaAs, 12% for CdTe, 3% for InAs, 2% for CdSe, and 1% for InP. It is important to point out that there are some uncertainties in the literature, especially for InSb. Interestingly, a g-factor of -58 ± 1 was experimentally reported for InSb nanowires, which largely exceeds the bulk limit that is usually reported in the literature (Table I) [76]. Our results confirm that such large g-factors are possible since we find a larger bulk value of −62.7.

In the case of GaAs, we have considered other tight-binding parameters, for comparison. We obtain $g_{\text{bulk}} = -0.123$ with the parameters of Ref. [77], and $g_{\text{bulk}} = -0.125$ with those of Ref. [78]. We conclude that all GaAs tight-binding parameters at our disposal (for a band structure at 0 K) give very consistent results. Therefore the origin of the discrepancy (15%) remains unclear even if some part is probably intrinsic to the semiempirical TB method (e.g., incomplete atomic basis). However, if we consider the mean error on $|g_{\text{bulk}} - g_0|$ for all compounds, we can conclude that the TB method provides a good description of the electron g-factors in semiconductors, even if it was not originally developed for that purpose.

For the sake of comparison with experiments, we can simply assume that the error on the g-factors made in TB will be the same in nanostructures as in bulk. This assumption will be validated in Sec. V D in the case of GaAs and CdTe.

IV. SPHERICAL QUANTUM DOTS

Figure 1 shows the electron g-factors obtained for spherical nanocrystals. They exhibit a clear dependence on the size of

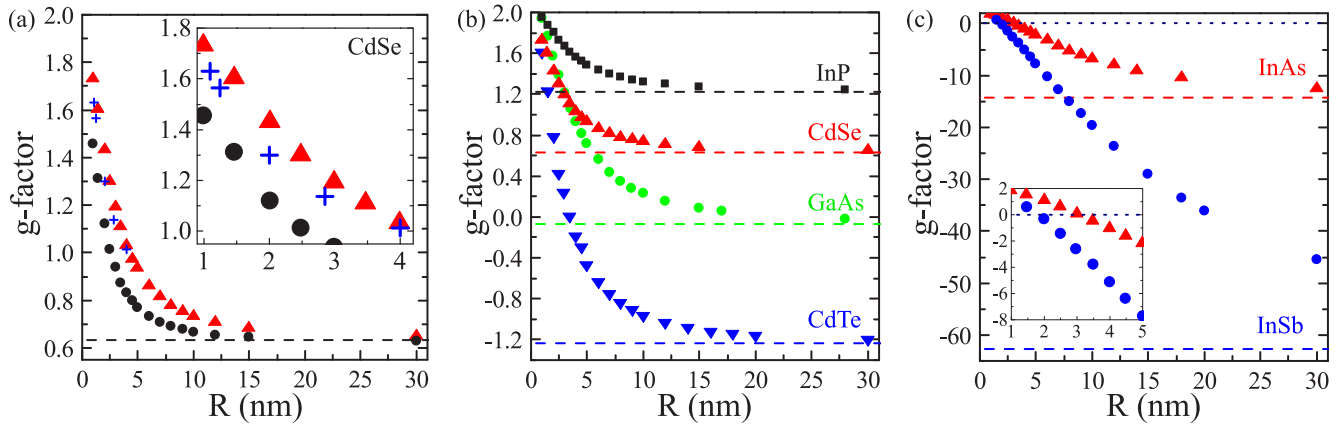

FIG. 1. Evolution of the electron g-factor in spherical semiconductor nanocrystals vs radius. (a) Results for CdSe nanocrystals (red ▲). The tight-binding values are compared to those obtained by Eq. (3) (black ●). The crosses represent the experimental data of Ref. [45]. The inset shows a zoom in on the small radius region. (b) Results for InP (black ■), CdSe (red ▲), GaAs (green ●), and CdTe (blue ▼) nanocrystals. (c) Results for InAs (red ▲) and InSb (blue ●) nanocrystals. The inset shows a zoom in around 0. The dashed line represents the calculated bulk value g_{bulk}. The dotted line indicates a null g-factor. The numerical values of the data presented in these figures are provided in Ref. [65].

the nanocrystal for all compounds. We show for comparison the values obtained for the bulk semiconductors.

The deviation of g from g_0 can be explained by the following arguments [56]. In bulk, the lowest conduction band state has a pure s character at $\mathbf{k} = 0$ but acquires components on p atomic orbitals at $\mathbf{k} \neq 0$. For example, in the $\mathbf{k}\cdot\mathbf{p}$ model of Kane, this mixing results from interband coupling characterized by the quantity E_p [46,47]. In nanocrystals, the localization of the wave function in real space leads to a delocalization in $\mathbf{k}$ space that brings p character to the wave function, which itself is influenced by the spin-orbit coupling. This gives a nonzero term $\langle\Psi_{c\uparrow}|l_z|\Psi_{c\uparrow}\rangle$ in Eq. (1).

The dependence on the size can be understood as follows. On the one hand, when the radius of the nanocrystal tends to zero, the orbital angular momentum is quenched ($\langle\Psi_{c\uparrow}|l_z|\Psi_{c\uparrow}\rangle \approx 0$) and the g-factor tends to a value close to g_0 [62,79]. On the other hand, when the size is increased, the g-factor tends to g_{bulk}. In the case of InSb, a huge variation is obtained. Figure 1(c) shows that the g-factor does not reach g_{bulk} even for a diameter of 60 nm. Moreover, for compounds with negative g_{bulk}, there exists a radius for which the Zeeman splitting vanishes [Figs. 1(b) and 1(c)]. A null electron g-factor is interesting for coherent photon-to-spin conversion in quantum bits [80,81]. We predict that it takes place for a diameter of 7.0 nm for CdTe, 48.0 nm for GaAs, 6.0 nm for InAs and 4.0 nm for InSb. For CdSe, our g-factors are in excellent agreement with the experimental data of Ref. [45] [Fig. 1(a)]. They are also in good agreement with the theoretical work of Rodina *et al.* [42] (not shown).

Figure 1(a) also presents a comparison between our calculated electron g-factors and the values given by the expression derived by Kiselev *et al.* [40],

$$g = g_0 - \frac{2E_p\Delta_{\text{SO}}}{3\left(E_g^b + E\right)\left(E_g^b + E + \Delta_{\text{SO}}\right)} \tag{3}$$

where E_g^b is the bulk energy gap, E is the electron energy with respect to the conduction band minimum (the confinement energy), and Δ_{SO} is the spin-orbit energy (splitting between heavy-hole and split-off valence bands). In the bulk limit ($E = 0$), Eq. (3) coincides with the Roth-Lax-Zwerdling relation [63]. The values of interband coupling matrix element E_p (Table I) calculated using the tight-binding approach are consistent with the literature [64,67,69,71]. Figure 1 shows that Eq. (3) in which we inject the tight-binding values for E_g^b, E_p, E (function of the size), and Δ_{SO} gives the correct trend for the evolution of the g-factor with the nanocrystal radius but there are important discrepancies. This shows the limits of the Kane model for the calculation of the g-factors.

V. UNIVERSALITY OF THE BEHAVIOR

Even though in the previous section the results were plotted versus the radius of the nanocrystals, it is not the main parameter that governs the evolution of the g-factor with size. We will show in the rest of this work that the main parameter is the energy gap, and that a universal behavior can be found among electron g-factors for all nanostructures of different shape and dimensionality. Figures 2 and 3 show the electron g-factors of all studied systems compared to the 0D spherical case (hereafter, the reference curve).

A. Universal expression for the reference curves

We have found that the reference curves for the different compounds are very well described by a surprisingly simple expression:

$$g(E_g) = \tilde{g}_0 - (E_0/E_g)^2, \tag{4}$$

where the parameters $\tilde{g}_0$ and E_0 are given in Table I. Figure 2 shows that the quality of the fit, realized on the g-factors for spherical nanocrystals, is excellent. Small discrepancies only appear for the smallest nanocrystals characterized by the largest energy gap. Remarkably, Eq. (4) calculated for E_g^b, the bulk value, gives a g-factor very close to g_{bulk}, whereas it was not considered in the fitted data.

The deviation of $\tilde{g}_0$ from g_0 shows that, even though the energy gap reaches very high values, the electron in the lowest conduction state does not behave as a free electron even if its wave function has a vanishing component on the Bloch states

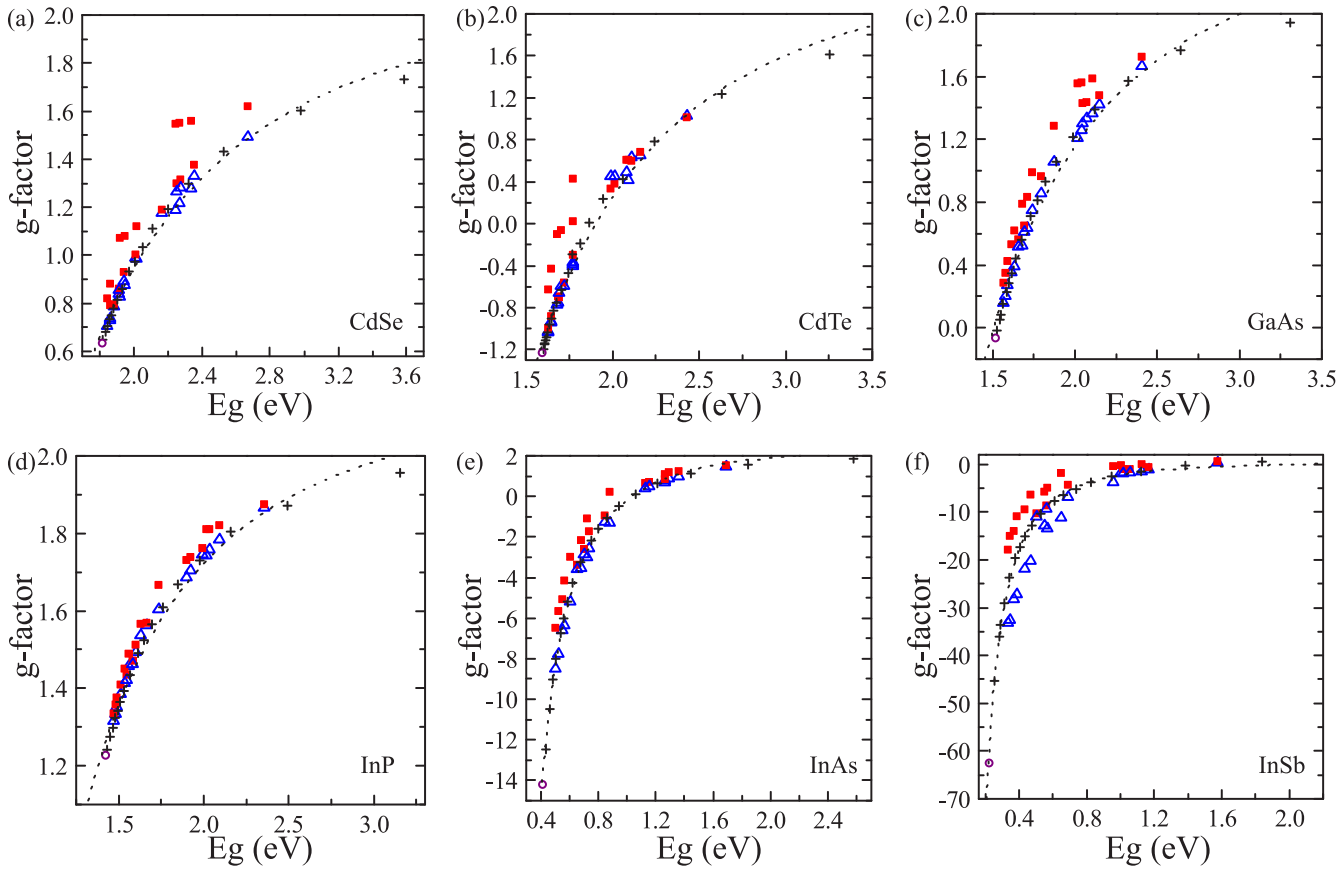

FIG. 2. Evolution of the electron g-factors vs the energy gap in systems characterized by a rotational symmetry axis (z), quantum wells, circular nanoplatelets and cylindrical nanorods (blue △ for g_z, red ■ for g_x). The results are shown for CdSe (a), CdTe (b), GaAs (c), InP (d), InAs (e), and InSb (f). The values for spherical nanocrystals are reported by black crosses and g_{bulk} is reported by purple ○. The numerical values of the data presented in these figures are provided in Ref. [65]. Dotted curves: g-factor vs energy gap given by Eq. (4) and the parameters of Table I.

of the valence band. In this limit of very strong confinement, the electron wave function is mainly derived from high-energy conduction states of the bulk which have an important weight on p atomic orbitals and is therefore influenced by the spin-orbit coupling.

In the following, we present the results for nanostructures with different dimensionality, shape, and size. The obtained g-factors are in many cases close to the reference curve. We identify the situations where the g-factors are the closest, and those where the deviations are larger. For this purpose, we separate the structures in two categories, those with or without a rotational symmetry axis.

B. Structures with rotational symmetry

Figure 2 shows the results for the structures characterized by a rotationally symmetric shape (discarding the atomic lattice), namely, quantum wells, circular platelets and cylindrical nanorods. We plot the values along the rotational symmetry axis with triangles, and those along the other directions with squares. It is clear that the g-factors along the rotational symmetry axis are in excellent agreement with the reference curve. As a consequence, the deviations from the reference curve of the g-factors along the other directions essentially result from anisotropies ($|g_x - g_z| \neq 0$). In many cases, the relative anisotropy that we characterize by the ratio $\Delta\tilde{g} = |g_x - g_z|/|g_0 - g_{\text{bulk}}|$ is small enough so that anisotropies can be neglected in first approximation. The amplitude of these anisotropies will be discussed in Sec. VI.

The largest deviations of g_z from the reference curve and the largest anisotropies are obtained for InSb quantum wells [Fig. 2(f) and Ref. [65]). Reasons will be discussed in Sec. VI.

It is important to point out that, among all semiconductor nanostructures that can be presently synthesized, most of them exhibit a rotational symmetry axis. This is the case in quantum wells, and in the large majority of nanorods and nanowires. The lateral sizes of the nanoplatelets are usually so large that these nanostructures can be safely considered as quantum wells [8]. In that cases, our results show that the electron g-factors along the symmetric axis can be predicted from the reference curve in a straightforward manner. The reference curve also provides a first estimate for the g-factors in the other directions.

C. Structures without rotational symmetry

Figure 3 presents the results for the structures without rotational symmetry, namely, nanocubes, square nanoplatelets, and nanorods with a square section. These results show that, when the rotational symmetry is broken, the deviations from the spherical case tend to become slightly more important but

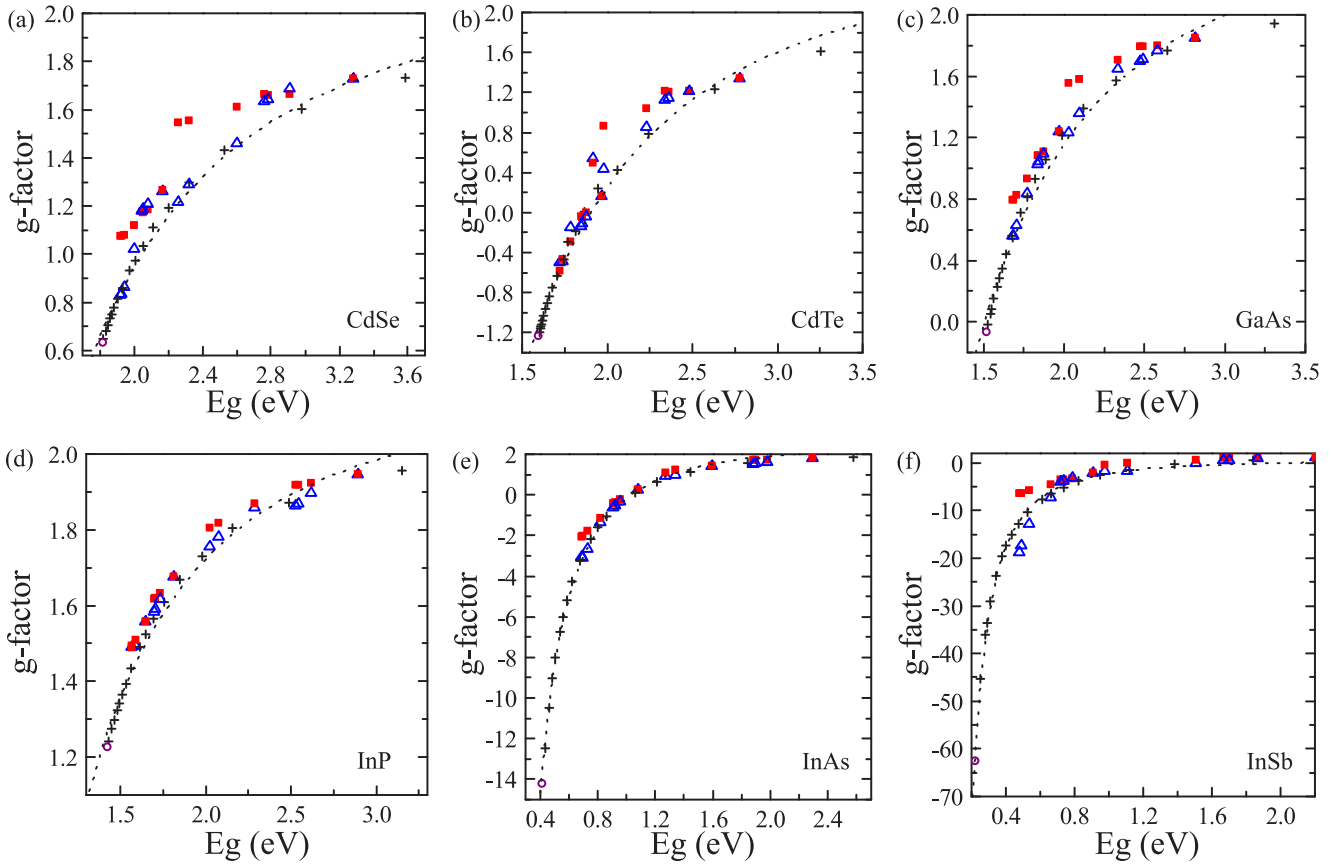

FIG. 3. Same as Fig. 2 for nanocubes, square nanoplatelets, and square nanorods (blue △ for g_z and red ■ for g_x). The numerical values of the data presented in these figures are provided in Ref. [65].

the variation versus the energy gap follows a similar trend. The deviations from the reference curve vary from structure to structure but happens in many cases to be quite small.

D. First experimental validations

In this section, we compare our predictions with available experimental data for InAs, GaAs, CdTe, and InP.

1. InAs

Recently, the electron g-factors of InAs circular disks embedded in InP were measured [50]. Even though InP cannot be considered as an infinite barrier material for electrons in InAs (band offset of 0.6 eV), it is nevertheless interesting to compare the reported values to the reference curve determined for InAs spherical nanocrystals [Fig. 4(a)]. An excellent agreement of the out-of-plane g-factor is found (along the rotational axis of the disk), and the anisotropy in those structures comes from the deviation of the in-plane values. Therefore these experimental results fully confirm our predictions of Sec. V.

Figure 4(a) also presents g-factors calculated for InAs disks embedded in InP. In order to study the evolution of the g-factors with the energy gap, we have considered several configurations in which the thickness and the diameter of the InAs disks are varied in a range compatible with experiments (details in Ref. [65]). We have included the effects on the electronic structure of strains induced by the lattice mismatch between InP and InAs. Details are described in Ref. [88]. The calculated g-factors are in very good agreement with experiments, for both out-of-plane and in-plane values. The anisotropy of the g-factors is correctly reproduced. The effects of strains on the g-factors are found to be small but not negligible—at most the correction on g is of order of 0.3 (see the same figure as Fig. 4(a) but without strain effects in Ref. [65]).

2. GaAs

We have also performed calculations of the electron g-factors in GaAs/$Al_{0.3}Ga_{0.7}As$ quantum wells of varying well thickness [Fig. 4(b)]. Since the conduction band offset between GaAs and $Al_{0.3}Ga_{0.7}As$ is small (0.24 eV), the range of variation of the energy gaps, and therefore of the g-factors, is rather limited. Once again, the values of g_z are in excellent agreement with the reference curve, especially at small energy, when the electron wave function is the most localized in the GaAs quantum well.

In order to compare with the experimental data, we shift the calculated g-factors for the quantum wells to take into account the discrepancy between calculated and experimental values for g_{bulk} (Sec. III). After correction, the agreement between theory and experiments is good [Fig. 4(b)] (see also the comparison with other experimental data in Ref. [65]). This result suggests that, for future use, the reference curve can be safely shifted by the same amount for comparison with experiments. Our calculations thus support the universal dependence of the out-of-plane g-factor on the lowest band-to-

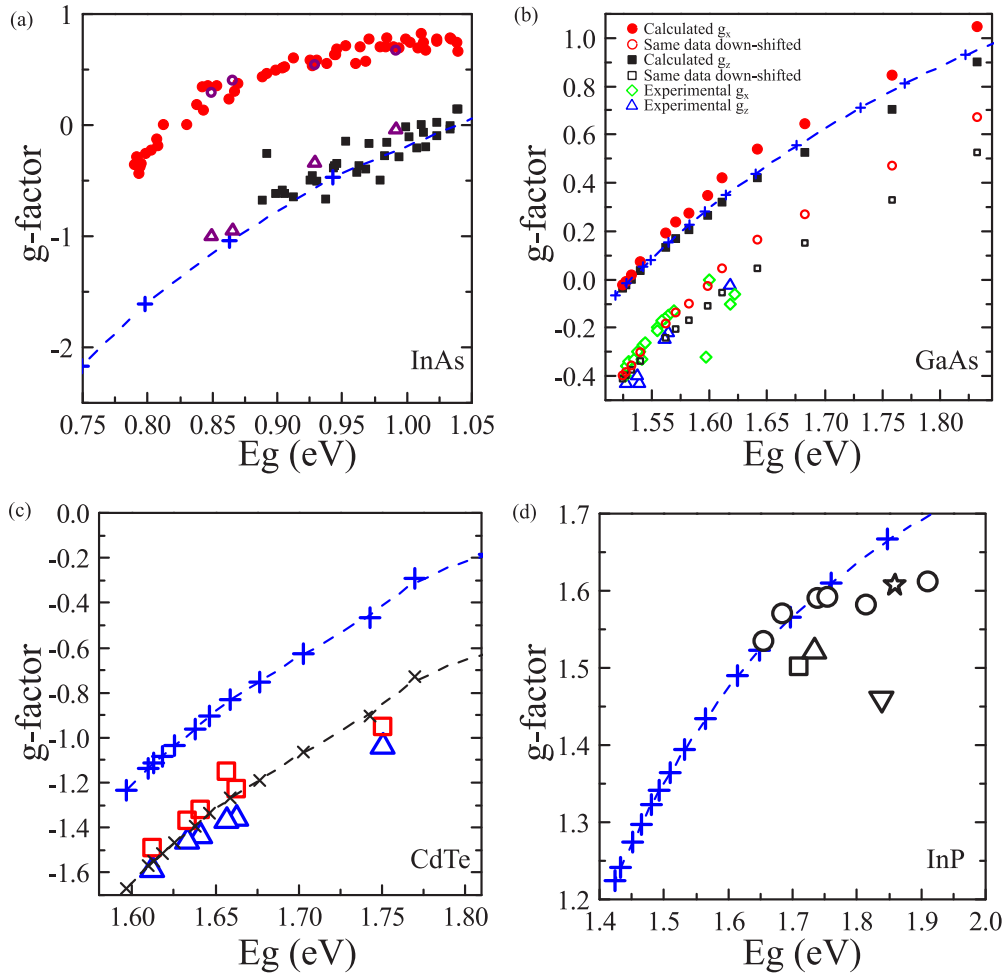

FIG. 4. Comparison between experimental and theoretical g-factors vs energy gap, for different systems. In (a)–(d), the blue crosses (+) connected by a dashed line represent the reference curves. (a) Results for InAs. Experimental values [50] of the out-of-plane [g_z] (black squares) and in-plane [g_x] (red disks) g-factors compared to our calculated data (purple triangles for g_z, purple circles for g_x), for InAs/InP disks. (b) Results for GaAs. Theory: g-factors for GaAs/$Al_{0.3}Ga_{0.7}As$ quantum wells (filled squares for g_z, red disks for g_x). Empty squares and red circles: same data down-shifted of 0.375 to account for the bulk error. Experimental data [48] for GaAs and AlGaAs quantum wells (blue triangles for g_z, green diamonds for g_x). (c) Results for CdTe. The black crosses (×) connected by a dashed line represent the reference curve down-shifted of 0.4245 to account for the bulk error. Experimental data of Ref. [82] for CdTe/$Cd_{1-x}Mg_xTe$ quantum wells (blue triangles for g_z, red squares for g_x). (d) Results for InP. Experimental results of Ref. [83] (star), Ref. [84] (circle), Ref. [85] (squares), Ref. [86] (△), and Ref. [87] (▽) for InP/GaInP quantum dots.

band optical transition energy in GaAs and AlGaAs quantum wells found in Ref. [48].

3. CdTe

Figure 4(c) presents experimental g-factors measured in CdTe/$Cd_{1-x}Mg_xTe$ quantum wells [82]. We are not able to perform TB calculations for this system due to the lack of TB parameters for the barrier material. However, it is interesting to see that these experimental data are close to the reference curve after correction of the bulk error in CdTe.

4. InP

In the case of InP [Fig. 4(d)], experimental data are available for InP/$Ga_{0.51}In_{0.49}P$ quantum dots. Some data at low energy are clearly in agreement with our reference curve. However, the important spread of the experimental values makes the comparison difficult. For transition energies around 1.9 eV, close to the band-gap energy of $Ga_{0.51}In_{0.49}P$, the penetration of the electron wave function into the barrier is probably important [89]. In addition, like for InAs/InP, the effects of strains on the electronic states are substantial in this system.

5. Validity and limits of the comparisons

It is important to recall that our predictions on the universality of the g-factor evolution concern strongly confined structures in which the surfaces behave as hard walls for the electron. The g-factors (and their anisotropy) will vary in a more complex way if the electron wave function overlaps regions of different composition or dimensionality [40,42,44]. This is already visible in the case of InAs/InP disks [Fig. 4(a)]. The values of g_z that we predict are slightly shifted from the reference curve, which is not the case for InAs disks with a high barrier at the surface. The same effect explains the small deviations of g_z from the reference curve for

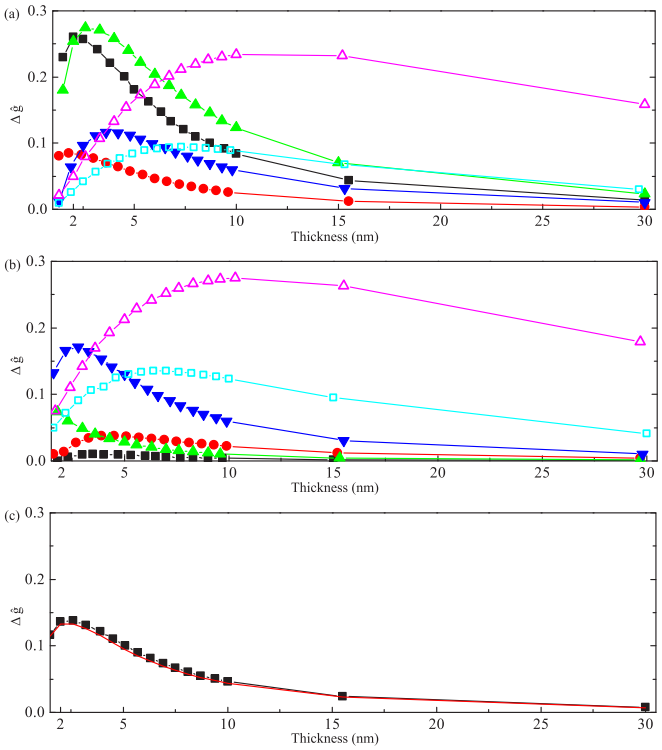

FIG. 5. Evolution of the relative amplitude of anisotropies $\Delta\tilde{g}$ in quantum wells vs their thickness. Results for CdSe (black ■), CdTe (green ▲), GaAs (blue ▼), InP (red ●), InAs (cyan □), and InSb (magenta △). (a) Results for quantum wells with surfaces terminated by anions. (b) Same for surfaces terminated by cations. (c) Results for CdSe quantum wells with one surface terminated by anions, the other by cations (black ■). The red line shows the average $\Delta\tilde{g}$ of CdSe quantum wells terminated by anions and cations.

$GaAs/Al_{0.3}Ga_{0.7}As$ quantum wells at high energy [Fig. 4(b)]. However, as GaAs and AlGaAs share a common anion that provides the dominant contribution to the spin-orbit coupling, the penetration of the electron wave function into the barrier has a small effect on the g-factors [48].

It is also important to point out that the in-plane component (g_x) has a much stronger dependence on the nature of the barrier material than the out-of-plane component (g_z). This point will be discussed in the next sections and in Appendix A.

Other experimental studies would be extremely useful to further support the universality of the reference curve. Studies on colloidal nanocrystals would be ideal since their surface capped with molecular ligands usually behaves as a high potential barrier.

VI. ANISOTROPIES

Clear anisotropies of the g-factors are observed in systems such as quantum wells. However, as already mentioned, the out-of-plane g-factor (g_z) is almost the same as in a sphere with the same energy gap. Indeed, it is the in-plane g-factor that mainly deviates from the reference curve. In this section, we quantify the g-factor anisotropies. The quantum well is taken as an example. Figure 5 shows the relative amplitude ($\Delta\tilde{g} = |g_x - g_z|/|g_0 - g_{\rm bulk}|$) of these anisotropies versus the thickness of the quantum wells.

We have found that $\Delta\tilde{g}$, through g_x, is highly sensitive to the surface passivation, especially in thin layers. This is demonstrated by plotting separately $\Delta\tilde{g}$ for quantum wells with surfaces terminated by anions [Fig. 5(a)] and cations [Fig. 5(b)]. For example, in CdSe and CdTe, when the surface planes are composed of Se(Te) atoms, the anisotropy is large [Fig. 5(a)]. On the contrary, the anisotropy almost vanishes for Cd-like surfaces [Fig. 5(b)]. Interestingly, the effect of each surface on $\Delta\tilde{g}$ is additive. $\Delta\tilde{g}$ for a quantum well terminated on one side by anions and on the other side by cations is equal to the half sum of $\Delta\tilde{g}$ of anion-terminated and cation-terminated quantum wells, as shown for CdSe in Fig. 5(c). This result unambiguously demonstrates that $\Delta\tilde{g}$ arises from surfaces. Such a dependence of the g-factors on the composition of the surface plane comes from surface components of the spin-orbit coupling [40,42] (see discussion in Sec. VII E). Experimentally, it was reported that the surface of CdSe and CdTe nanoplatelets is always Cd-like [90], therefore we expect small anisotropies.

It is interesting to see that the differences between anion- or cation-terminated quantum wells are reduced for GaAs, InP, InAs, i.e., when we have used the first surface passivation model in which the dangling bonds are saturated by pseudohydrogen atoms. As already discussed in Sec. II A, the first model describes a confinement potential at the surface smoother than in the second model used for InSb, CdSe, and CdTe. We have checked that the sensitivity to the surface is enhanced in GaAs, InP, and InAs when the second passivation model is used. Therefore our calculations confirm that the nature of the confinement potential has a visible influence on the g-factors of nanostructures [40,42,43]. In quantum wells (or nanoplatelets), this sensitivity is considerably stronger for g_x (in-plane) than for g_z (out-of-plane).

Figure 5 also shows that, in any case, $\Delta\tilde{g}$ tends to decrease for larger thickness, when the electronic wave functions are less sensitive to the surface and the magnetic-field-induced effects of the spin-orbit coupling on the conduction states tend to decrease. However, the overall behavior of $\Delta\tilde{g}$ versus thickness in InAs and InSb is clearly different from the others. In these compounds, the relative anisotropy first increases with size, reaches a maximum and then decreases. In the other semiconductors, the average relative anisotropy is continuously decreasing with size. The different behavior in InAs and InSb can be related to their small band gap in the bulk that results in stronger s-p (via E_p) and spin-orbit couplings in the conduction band.

Except for InSb quantum wells and thin CdSe (CdTe) quantum wells, the relative deviation $\Delta\tilde{g}$ is smaller than 0.15 (Fig. 5). This tells us that, in a first approximation, the reference curve can be used for most structures and field directions (for strongly confined nanostructures). It also indicates that, although the anisotropies take their origin from the anisotropic shape of the nanocrystal, their larger values in InAs and InSb ($|g_x - g_z|$ up to 18) mainly come from the large deviation of $g_{\rm bulk}$ from g_0, and not from the differences between the dimensions of the nanocrystal. This is clearly visible in Figs. 2 and 3 where all the obtained values are close to the reference curve when they are plotted in the range $[g_{\rm bulk}, g_0]$.

VII. INSIGHT INTO THE UNIVERSALITY OF THE REFERENCE CURVE

We can conclude from the tight-binding calculations that the evolution of the electron g-factor versus the energy gap is to a large extent shape-independent. The universality of the reference curve is particularly striking along the rotation symmetry axis of the nanostructure when it exists.

It remains to understand the physical origin of these results. From the literature, we can already notice that the g-factors in quantum wells, nanowires, and quantum dots can be given by a same function of the confinement energy of the ground state electron when surfaces behave as infinite barriers [Eq. (3)] [40,44]. However, this result was obtained on the basis of the Kane model. In addition, the physical reasons why the expression for the g-factor is the same in the three systems is not clear. Our calculations show that remote band effects (beyond Kane model) and deviations from Eq. (3) are important but the reference curve works for many different types of semiconductor nanostructures. Therefore this universal behavior of the g-factors must be based on robust physical arguments that we investigate in the remaining part of this section.

A. General arguments

From the comparison between Eqs. (1) and (4), we deduce from our calculations that the matrix element $\langle\Psi_{c\uparrow}|l_z|\Psi_{c\uparrow}\rangle$ of the orbital momentum varies as $1/E_g^2$. In addition, for a fixed energy gap, and for z along a rotational axis of a 0D nanostructure, the universality of the reference curve demonstrates that the matrix element does not depend on the lateral extension of the wave function since the same g-factor is found for spheres, cylindrical nanorods, and nanoplatelets. The same conclusion holds in extended systems such as quantum wells, nanowires and bulk, if we use for $\Psi_{c\uparrow}$ any spin-up eigenfunction of the Hamiltonian with rotational symmetry, for example, the wave function corresponding to a quantized cyclotron orbit. In line with this statement, the g-factor that characterizes the Zeeman splitting in semiconductor quantum wells is usually assumed to be the same for all Landau levels, whatever the magnitude of the applied magnetic field. The fact that Eq. (4), obtained by fitting the g-factors for spherical nanocrystals, tends naturally to g_{bulk} for $E_g = E_g^b$ shows that the physical origin of the electron orbital momentum is the same from small nanostructures to the bulk. This is not a trivial fact if we consider the strong effect of the quantum confinement on the electron wave functions.

B. Spin-orbit-induced currents

We conclude from the previous discussion that the g-factor for an electron is, to a large extent, independent of its wave function $\Psi_{c\uparrow}(\mathbf{r})$ and is just determined by the energy gap E_g. This must be true whatever the size, the shape and the dimensionality (0D–3D) of the system (neglecting anisotropies for the moment). In this context, it is interesting to decompose the magnetic moment $\boldsymbol{\mu}$ of the electron into its contributions from each unit cell n of the material,

$$\boldsymbol{\mu} = \sum_n \boldsymbol{\mu}(\mathbf{r}_n) = \sum_n [\boldsymbol{\mu}_s(\mathbf{r}_n) + \boldsymbol{\mu}_l(\mathbf{r}_n)], \tag{5}$$

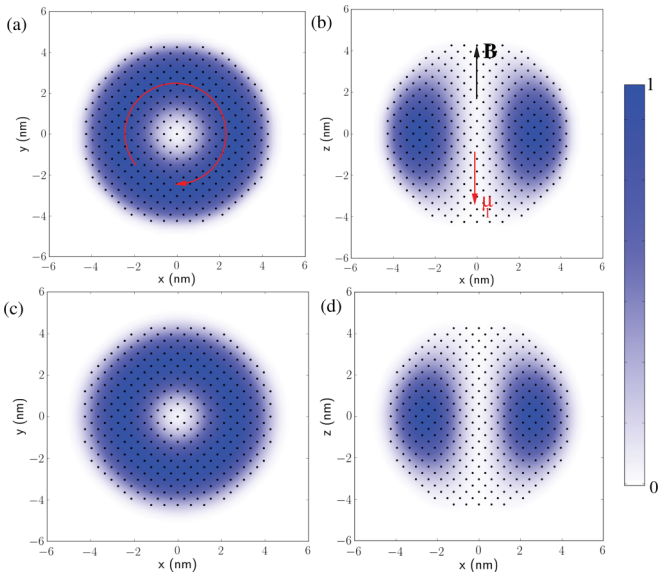

FIG. 6. Normalized density of $g_0 - g_z$ on each atom of a spherical nanocrystal of CdSe (diameter = 9 nm) for a magnetic field along z. The density is shown in the xOy (a) and xOz (b) planes passing through the center of the sphere. These data can be seen as the intensity of the local orbital component $\boldsymbol{\mu}_l(\mathbf{r})$ of the magnetic moment (red arrow) induced by the circulating current [depicted by the circular arrow in (a)] generated by the spin-orbit coupling. The atoms are represented by black dots. (c) and (d) are same as (a) and (b), respectively, but calculated using the analytic envelope wave function (Appendix B).

where $\boldsymbol{\mu}_s(\mathbf{r})$ and $\boldsymbol{\mu}_l(\mathbf{r})$ are the spin and orbital components of the local moment, respectively, and $\mathbf{r}_n$ is the vector pointing to the unit cell n. The spin component $\boldsymbol{\mu}_s(\mathbf{r})$, at the origin of g_0 in the g-factor, is just proportional to $|\Psi_{c\uparrow}(\mathbf{r})|^2$ [49]. The wave function being normalized, the total spin moment $\boldsymbol{\mu}_s$ is equal to $-\mu_B g_0 \mathbf{s}/\hbar$, whatever $\Psi_{c\uparrow}$.

It is thus tempting to apply the same reasoning for the orbital component $\boldsymbol{\mu}_l(\mathbf{r})$. However, as shown in Ref. [49], $\boldsymbol{\mu}_l(\mathbf{r})$ is not proportional to $|\Psi_{c\uparrow}(\mathbf{r})|^2$ because the orbital moment comes from circulating orbital currents produced by the spin-orbit coupling, resulting in a complex spatial structure of $\boldsymbol{\mu}_l(\mathbf{r})$. This is clearly visible in Figs. 6 and 7 where we plot the normalized orbital moment $\boldsymbol{\mu}_l(\mathbf{r})$ calculated in the tight-binding approximation for a spherical nanocrystal and a circular nanoplatelet, respectively. In both cases, the spatial structure of the local magnetic moment results from a spin-orbit-induced current looping around the magnetic field axis centered on the nanostructure. A very similar result was obtained in Ref. [49] for a spherical quantum dot treated in the envelope function approximation. The orientation of the electron spin determines the direction of the current flow. The shape and the extension of the current loop strongly depend on the geometry of the nanostructure [50]. For example, in the circular nanoplatelet in which we apply a in-plane magnetic field [Fig. 7(b)], the current loop is constrained by the small thickness of the platelet and therefore the loop has a rectangular shape instead of a ring shape found for the spherical nanocrystal (Fig. 6). In these conditions, it is not

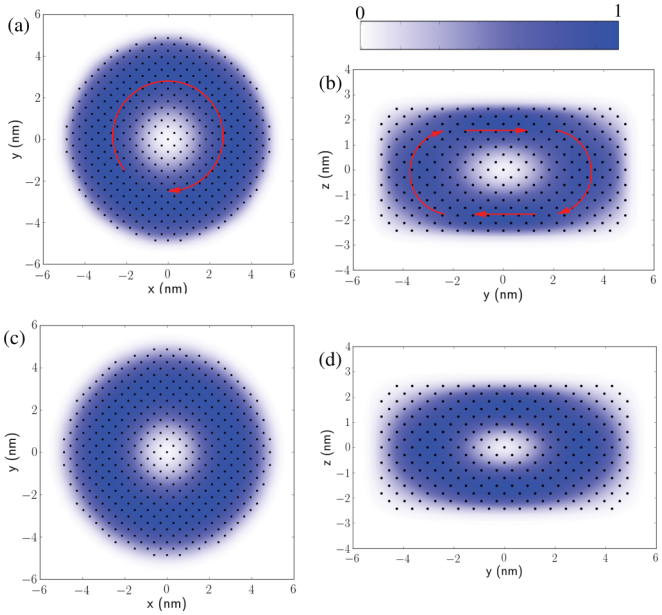

FIG. 7. Same as Fig. 6 but for a circular nanoplatelet (diameter = 10 nm, thickness = 5 nm). (a) Density of $g_0 - g_z$ in the xOy plane when the magnetic field is along z, the rotational symmetry axis of the nanoplatelet. (b) Density of $g_0 - g_x$ in the yOz plane for the magnetic field along x. (c) and (d) are same as (a) and (b), respectively, but calculated using the analytic envelope wave function (Appendix B).

trivial to understand why the total moment given by Eq. (5) does not depend on the electron wave function.

C. Approximate analytic expression for the orbital magnetic moment

In this section, we derive an expression for the orbital magnetic moment and for the g-factors using analytical developments based on a $\mathbf{k}\cdot\mathbf{p}$ theory. In the next section, we generalize the obtained formulas and we validate them against tight-binding calculations. We explain why the orbital magnetic moment of the electron is strongly dependent on the wave function at the local level but becomes to a large extent invariant when integrated over the system.

We consider for the moment a finite system (0D). All information concerning the g-factor and the spin-orbit-induced current is included in the wave function $\Psi_{c\uparrow}(\mathbf{r})$ (Sec. II B 1). For a nanostructure much bigger than a unit cell along its three dimensions, we decompose its volume V into a surface region of volume V_{surf}, and the interior (of volume $V_{\text{in}} = V - V_{\text{surf}}$) that we define as the region in which $\Psi_{c\uparrow}(\mathbf{r})$ can be safely written in the envelope function approximation as [46,56,57]

$$\Psi_{c\uparrow}(\mathbf{r}) \approx \sum_i F_i(\mathbf{r}) u_i(\mathbf{r}), \tag{6}$$

where $F_i(\mathbf{r})$ is a spatially slowly varying envelope function. The sum in Eq. (6) runs over all Bloch states $u_i(\mathbf{r})$ of band i calculated for the bulk at $\mathbf{k} = 0$. For $\Psi_{c\uparrow}$, the main term involves the s-like Bloch state $u_{s\uparrow}$ that describes the crystal state of spin up at the bottom of the lowest conduction band. Smaller contributions come from the p-like Bloch states of the top of the valence band usually labeled $u_{x\uparrow}, u_{y\uparrow}, u_{z\uparrow}, u_{x\downarrow}, u_{y\downarrow}, u_{z\downarrow}$.

The orbital magnetic moment in the cell n is related to the orbital current density $\mathbf{j}(\mathbf{r}) = (e\hbar/m_0)\,\text{Im}\{\Psi^*_{c\uparrow}(\mathbf{r})\boldsymbol{\nabla}\Psi_{c\uparrow}(\mathbf{r})\}$ by

$$\boldsymbol{\mu}_l(\mathbf{r}_n) = \frac{1}{2}\int_{\text{cell}\,n} \mathbf{r}\times\mathbf{j}(\mathbf{r})\,d\mathbf{r}. \tag{7}$$

Using Eqs. (5)–(7), the orbital moment in V_{in} can be decomposed in different terms coming either from the Bloch velocity or the envelope velocity [49]. In addition, the orbital current within a unit cell n can be split into an itinerant contribution $\langle\mathbf{j}\rangle_n$ and a localized contribution $\mathbf{j}(\mathbf{r}) - \langle\mathbf{j}\rangle_n$ [91]. It was shown in Ref. [49], and confirmed by our calculations, that the dominant contribution to the magnetic moment of the electron comes from the itinerant current arising from the Bloch velocity

$$\boldsymbol{\mu}_l(\mathbf{r}_n) \approx -\mu_B V_0 \sum_{i\neq j} \text{Im}\{F_i^*(\mathbf{r}_n)F_j(\mathbf{r}_n)(\mathbf{r}_n \times \langle u_i|\boldsymbol{\nabla}|u_j\rangle)\} \tag{8}$$

in which V_0 is the unit cell volume, $\langle u_i|\boldsymbol{\nabla}|u_j\rangle$ is defined as $V_0^{-1}\int_{V_0} u_i^*(\mathbf{r})\boldsymbol{\nabla}u_j(\mathbf{r})d\mathbf{r}$, and we use the normalization condition $\int_{V_0}|u_i(\mathbf{r})|^2 d\mathbf{r} = V_0$. The terms with $i = j$ are excluded because $\langle u_i|\boldsymbol{\nabla}|u_i\rangle = 0$ [46].

In order to establish an expression for $\boldsymbol{\mu}_l$, the main challenge is to derive the envelope wave functions using a general approach that does not depend on the shape of the nanostructure. For this purpose, we work in the framework of the $\mathbf{k}\cdot\mathbf{p}$ theory [46,47,56]. A $\mathbf{k}\cdot\mathbf{p}$ model is defined by its basis set of Bloch states u_i. An effective Hamiltonian is written in this basis as $H = H_0 + H_{kp} + H_{\text{SO}}$ where H_{SO} is the spin-orbit coupling and $H_{kp} = \hbar\mathbf{k}\cdot\mathbf{p}/m_0$. H_0 is defined by parameters which are renormalized to include the effects of remote bands [46,47]. To describe conduction states like $\Psi_{c\uparrow}(\mathbf{r})$, it is in principle sufficient to work with the single Bloch state $u_{s\uparrow}$. In that case, $F_s(\mathbf{r})$ is just solution of the differential equation [46,56,57]

$$\left(-\frac{\hbar^2}{2m_e^*}\Delta + V_{\text{conf}}(\mathbf{r})\right)F_s(\mathbf{r}) = E_s F_s(\mathbf{r}), \tag{9}$$

where m_e^* is the effective mass in the conduction band and $V_{\text{conf}}(\mathbf{r})$ is the confining potential.

If we remain at this level of approximation, the orbital magnetic moment vanishes since the spin-orbit coupling only becomes effective in presence of p states. The next step is therefore to consider a $\mathbf{k}\cdot\mathbf{p}$ model, which includes the p-like Bloch states from the valence band maximum [47,56]. However, since the weight of $\Psi_{c\uparrow}(\mathbf{r})$ on p orbitals is small, it is sufficient to consider the coupling between s and p states described in H_{kp} at the first order in perturbation. Working in the reciprocal (Fourier) space, i.e., $F_s(\mathbf{r}) \to F_s(\mathbf{k})$ and $F_j(\mathbf{r}) \to F_j(\mathbf{k})$, we obtain [46,56]

$$F_j(\mathbf{k}) \approx \frac{\hbar}{m_0}\frac{\mathbf{k}\cdot\langle u_j|\mathbf{p}|u_s\rangle}{E_s^0 - E_j^0}F_s(\mathbf{k}), \tag{10}$$

where $E_j^0 = \langle u_j|H_0 + H_{\text{SO}}|u_j\rangle$ calculated at $\mathbf{k} = 0$. E_s^0 is E_j^0 for $j = s$. This first-order treatment of H_{kp} at $\mathbf{k}\approx 0$ is justified since the envelope functions are slowly variable in real space [46,56].

The main contributions in Eq. (8) are those with $F_i = F_s$ (or $F_j = F_s$) and nonzero matrix elements of the gradient

$\langle u_s|\nabla|u_j\rangle$ ($\langle u_i|\nabla|u_s\rangle$). Equation (8) is thus given by a sum of terms containing $F_j(\mathbf{k})$ on which we must apply an inverse Fourier transformation. Using $\mathbf{k}F_s(\mathbf{k}) \to -i\nabla F_s(\mathbf{r})$, Eq. (8) becomes

$$\boldsymbol{\mu}_l(\mathbf{r}_n) \approx 2\mu_B V_0 \frac{\hbar^2}{m_0} \sum_j \mathrm{Im}\left[F_s^*(\mathbf{r}_n) \frac{1}{E_s^0 - E_j^0} \times \nabla F_s(\mathbf{r}_n) \cdot \langle u_j|\nabla|u_{s\uparrow}\rangle (\mathbf{r}_n \times \langle u_{s\uparrow}|\nabla|u_j\rangle)\right], \quad (11)$$

where the factor 2 comes from the identical contributions of the terms with interchanged i and j in Eq. (8).

At this stage, it is better to consider a basis of Bloch states u_j in which $H_0 + H_{\mathrm{SO}}$ is diagonal at $\mathbf{k} = 0$ [56]. For the top of the valence band, these Bloch states can be written as $|J,M\rangle$, they form a quadruplet of energy $E_{3/2}$ characterized by a total angular momentum $J = 3/2$ of Γ_8 symmetry and a doublet of energy $E_{1/2}$ with $J = 1/2$ of Γ_7 symmetry. M is the projection of the total angular momentum along the z axis. We use the notations of Ref. [92] for the irreducible representations for the $T_d \times \Gamma_6$ double group. The energy separation between the multiplets, due to the spin-orbit coupling, is $\Delta_{\mathrm{SO}} = E_{3/2} - E_{1/2}$. The states $|J,M\rangle$ are expressed as linear combinations of the Bloch functions $u_{x\uparrow}$, $u_{y\uparrow}$, $u_{z\uparrow}$, $u_{x\downarrow}$, $u_{y\downarrow}$, $u_{z\downarrow}$ [56]. The nonzero matrix elements of the velocity operator are $P = -\hbar\langle u_s|\partial/\partial x|u_x\rangle/m_0$ (same for y and z). After some algebra, replacing the sum over n in Eq. (5) by an integral $V_0^{-1}\int_V d\mathbf{r}$, we obtain using $E_P = 2m_0P^2$ and $E_g^b = E_s^0 - E_{3/2}^0$:

$$\boldsymbol{\mu}_l \approx \frac{\mu_B}{3} \frac{E_P\,\Delta_{\mathrm{SO}}}{E_g^b\left(E_g^b + \Delta_{\mathrm{SO}}\right)} \begin{vmatrix} \int_V F_s^*(\mathbf{r}) z \frac{\partial}{\partial x} F_s(\mathbf{r}) d\mathbf{r} \\ \int_V F_s^*(\mathbf{r}) z \frac{\partial}{\partial y} F_s(\mathbf{r}) d\mathbf{r} \\ -\int_V F_s^*(\mathbf{r}) \left(x\frac{\partial}{\partial x} + y\frac{\partial}{\partial y}\right) F_s(\mathbf{r}) d\mathbf{r}. \end{vmatrix} \quad (12)$$

This equation holds for the electron spin oriented along z (spin up). The opposite is found for a spin down along z. For a spin along x or y, we obtain formally similar equations by permutation of the components, and of x, y, z. Interestingly, we can synthesize all results into a simple formula,

$$\boldsymbol{\mu}_l \approx -\frac{\mu_B}{3} \frac{E_P\,\Delta_{\mathrm{SO}}}{E_g^b\left(E_g^b + \Delta_{\mathrm{SO}}\right)} \langle F_s|\mathbf{r} \times (\mathbf{e}_s \times \nabla)|F_s\rangle, \quad (13)$$

where $\mathbf{e}_s$ is the orientation of the spin.

In the case of a spherical nanocrystal of radius R, the envelope wave function solution of Eq. (9) is equal to

$$F_s(\mathbf{r}) = \frac{1}{r\sqrt{2\pi R}} \sin\left(\frac{\pi r}{R}\right) \quad (14)$$

in spherical coordinates, for an infinite potential well. The x and y components of $\boldsymbol{\mu}_l$ vanish and the integral in the z component of Eq. (12) is equal to -1. If we add the spin magnetic moment $-\mu_B g_0/2$, we get the total magnetic moment that we write $-\mu_B g_z/2$. We deduce the g-factor

$$g_z = g_0 - \frac{2}{3} \frac{E_P\,\Delta_{\mathrm{SO}}}{E_g^b\left(E_g^b + \Delta_{\mathrm{SO}}\right)}, \quad (15)$$

which corresponds exactly to the Roth-Lax-Zwerdling relation [63].

In fact, this result is universal in the sense that it does not depend on F_s. It is easy to check, by integration by parts of a normalized function, that the integral in the z component of Eq. (12) is always equal to -1, whatever the wave function F_s. The integrals in x and y components always vanish for any normalizable wave function. Therefore Eq. (15) remains valid whatever the shape of the nanostructure.

D. General expressions for the magnetic moment and the g-factors

The important conclusion of the previous section is that the Roth-Lax-Zwerdling relation [Eq. (15)] can be established for nanostructures with arbitrary shape. At the same time, the derivation of this equation is based on approximations, on a simple $\mathbf{k}\cdot\mathbf{p}$ model and a first-order perturbative treatment. As a consequence, Eq. (15) does not give the correct values for the g-factors. However, we have discovered that the universal law given by Eq. (12) describes the results of our tight-binding calculations very well, except that the prefactor in front of the integrals must be modified in order to reproduce the g-factors calculated numerically.

Therefore, in the following, we propose general expressions for the magnetic moment and the g-factors of an electron in an arbitrary III-V or II-VI semiconductor nanostructure. First, we formulate them. Second, we discuss their main properties. Third, we justify them using general physical arguments. Fourth, we validate them against the tight-binding calculations.

1. Formulation of the main results

The main conclusions of our work are summarized here. Based on the results discussed in the previous sections, we propose the following expressions for the total magnetic moment:

$$\boldsymbol{\mu} = -\frac{1}{2}\mu_B g_0 \mathbf{e}_s + \boldsymbol{\mu}_{\mathrm{surf}} + \frac{1}{2}\mu_B \left[\tilde{g}_0 - g_0 - \left(\frac{E_0}{E_g}\right)^2\right] \times \langle F_s|\mathbf{r} \times (\mathbf{e}_s \times \nabla)|F_s\rangle, \quad (16)$$

and for the g-tensor

$$[g] = g_0[I] + [g_{\mathrm{surf}}] - \left[\tilde{g}_0 - g_0 - \left(\frac{E_0}{E_g}\right)^2\right] \langle F_s|[\Xi]|F_s\rangle \quad (17)$$

with

$$[\Xi] = \begin{bmatrix} y\frac{\partial}{\partial y} + z\frac{\partial}{\partial z} & -y\frac{\partial}{\partial x} & -z\frac{\partial}{\partial x} \\ -x\frac{\partial}{\partial y} & x\frac{\partial}{\partial x} + z\frac{\partial}{\partial z} & -z\frac{\partial}{\partial y} \\ -x\frac{\partial}{\partial z} & -y\frac{\partial}{\partial z} & x\frac{\partial}{\partial x} + y\frac{\partial}{\partial y} \end{bmatrix}. \quad (18)$$

$[I]$ is the identity tensor. The vector $\mathbf{e}_s$ in Eq. (16) indicates the orientation of the electron spin. $\boldsymbol{\mu}_{\mathrm{surf}}$ is an implicit function of $\mathbf{e}_s$. The electron envelope wave function F_s is solution of Eq. (9). $\tilde{g}_0$ and E_0 are given in Table I.

In Eqs. (16) and (17), the first term is related to the spin magnetic moment, the second and third ones to the spin-orbit induced orbital magnetic moment. The second term, unspecified in the present work, comes from magnetic moments

specifically induced by the surface of the nanostructure. By contrast, the third term can be designated as the bulk term.

Since all nondiagonal matrix elements of $[\Xi]$ vanish, the g-tensor simplifies into

$$[g] = \left[\tilde{g}_0 - \left(\frac{E_0}{E_g}\right)^2\right][I] + [g_{\text{surf}}]. \tag{19}$$

Consequently, in absence of surface term, the g-factor is isotropic and follows a universal rule that just depends on the energy gap of the system. This rule is valid from 0D nanostructures to bulk.

2. Main features of the general expressions

From Eq. (16), we see that the local orbital magnetic moment $\boldsymbol{\mu}_l(\mathbf{r})$ inside the nanostructure, being proportional to $F_s^*(\mathbf{r})[\mathbf{r} \times (\mathbf{e}_s \times \boldsymbol{\nabla})]F_s(\mathbf{r})$, is strongly dependent on F_s and therefore on the shape and the size of the nanostructure. However, the matrix elements $\langle F_s|x\frac{\partial}{\partial x}|F_s\rangle$, $\langle F_s|y\frac{\partial}{\partial y}|F_s\rangle$, and $\langle F_s|z\frac{\partial}{\partial z}|F_s\rangle$ are all equal to $-1/2$, whatever the wave function F_s. The diagonal matrix elements of Ξ are all equal to -1. All nondiagonal matrix elements of Ξ vanish. Therefore the g-factor is fully isotropic in absence of surface terms, whatever the shape, the size, and the dimensionality of the system [Eq. (19)]. In other words, anisotropies only come from surface terms. This is once again consistent with our previous conclusions, in particular of Sec. VI. For all these reasons, the prefactors in front of the matrix elements in Eqs. (16) and (17) have been defined in such way that, in absence of surface terms, the expression of the diagonal g-factors in Eq. (19) coincides with Eq. (4) derived from the tight-binding calculations.

3. Justification of the general expressions

Equations (12) and (13) have been established on the basis of a $\mathbf{k}\cdot\mathbf{p}$ model. The form of the operators present in the integrals of Eq. (12), i.e., in the bulk term, is the resultant of two factors. First, the s-like conduction Bloch states are coupled to the p_x-like valence Bloch states by a term proportional to k_x in the reciprocal space (via P), leading to an envelope wave function on p_x states proportional to $\frac{\partial}{\partial x}F_s$ (idem for y and z). Second, for a spin along z, the electron hops between p_x and p_y atomic orbitals due to the spin-orbit coupling, the direction of motion depending on the orientation of the spin. This leads to a spin-orbit induced current $\mathbf{j}$ along y for p_x orbitals, along x for p_y orbitals. It gives a magnetic moment ($\propto \mathbf{r}\times\mathbf{j}$) along z of the form $F_s^*(\mathbf{r})(x\frac{\partial}{\partial x} + y\frac{\partial}{\partial y})F_s(\mathbf{r})$ as found in Eq. (12).

Formally, it should be possible to calculate the g-factors using an improved methodology by adding Bloch states in the basis of the $\mathbf{k}\cdot\mathbf{p}$ model and by going to higher order in perturbation [93,94]. For example, a better but still approximate treatment could lead to the formula of Kiselev *et al.* [40], Eq. (3). Beyond that, remote band effects could be described in principle by projection techniques [46,95]. However, this requires heavy analytic developments. Our tight-binding calculations have shown that all these effects bring non-negligible corrections to the g-factors (Sec. IV). To account for these effects, we have thus modified the prefactor in front of the integrals in Eq. (12), which leads to Eq. (16). However, the operators inside the integrals remain the same for the following reasons.

If we add more Bloch states in the $\mathbf{k}\cdot\mathbf{p}$ model, the envelope wave functions F_j for $j \neq s$ will still be given at the first order by a term proportional to $\mathbf{k}\cdot\mathbf{p}$. For symmetry reasons, the matrix elements $\langle u_s|\partial/\partial x|u_j\rangle$ only couple the state u_s of Γ_6 symmetry to the states u_j of Γ_7 and Γ_8 symmetry that behave as x (respectively, for y and z) [94]. Therefore the total envelope wave function related to x orbitals will remain proportional to $\frac{\partial}{\partial x}F_s$. In addition, the effect of the spin-orbit coupling in a sector of Bloch states u_j that behave as x, y, and z can still be mapped on the basis of the $|J,M\rangle$ states. Therefore all rules used to establish the integrals in Eq. (12) remains valid, only the prefactor changes.

As discussed in Sec. VII C, the envelope function approximation is only justified in the interior volume of the nanostructure (V_{in}). The modifications of the electron wave function near the surface (in V_s) with respect to its expression of Eq. (6) may be quite important. These effects modify locally the spin-orbit induced current and the orbital magnetic moment. In Eq. (16), this is simply described in $\boldsymbol{\mu}_{\text{surf}}$. For the same reasons, strictly speaking, the integrals in Eqs. (12), (16), and (17) should be made over the volume V_{in}. However, it is always possible to integrate over the full volume V and to put the corrections in the surface term. This is the procedure that we followed to derive Eqs. (16) and (17).

4. Validation of the general expressions

The universality of the reference curve is already a solid argument to validate our expressions for the magnetic moment and the g-factors since the universality is directly connected to the invariance of the integrals in Eqs. (16) and (17) with respect to the electron wave function.

We have also performed more quantitative comparisons between analytic and tight-binding calculations. We have computed the local orbital magnetic moment $\boldsymbol{\mu}_l(\mathbf{r})$ for different types of nanostructures from Eq. (16) using envelope wave functions $F_s(\mathbf{r})$. Two examples of results are presented in Figs. 6 and 7, for a spherical nanocrystal and a circular nanoplatelet, respectively. The corresponding analytic expressions of the orbital magnetic moment density are given in Appendix B. In both cases, the agreement between analytic and tight-binding calculations is excellent. This demonstrates that spin-orbit induced currents are correctly described by our formula. This is remarkable since everything is deduced from a simple envelope wave function. A deeper analysis of the data presented in Figs. 6 and 7 shows that the discrepancy between analytic and tight-binding results is below 5%, except for small terms at the surface, which was expected.

E. Surface terms

The present study was focused on the universal behavior of the g-factors, therefore on the bulk contribution. Further work is clearly needed for a deeper investigation of the surface term. This latter may have two different origins. First, deviations from Eq. (8) are expected in the region close to the surface (in V_{surf}) where the envelope function approximation progressively breaks down. In other words, the full wave function $\Psi_{c\uparrow}(\mathbf{r})$ is composed of bulk components

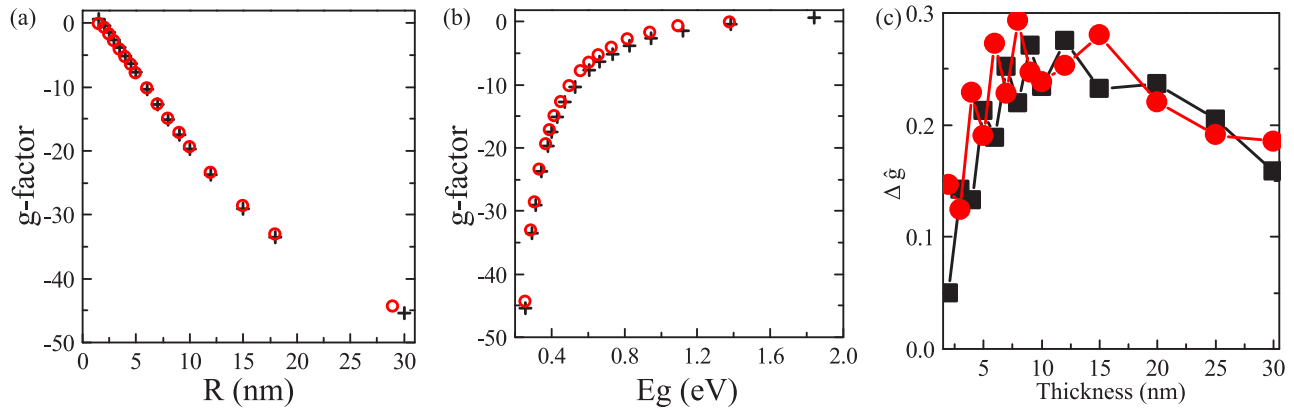

FIG. 8. Effect of the confining barrier height on the electron g-factor. (a) and (b) Results for InSb spherical nanocrystals with an infinite barrier (black crosses) and with a finite one (InSb/CdTe core-shell nanocrystals, red ○). The results are plotted vs the radius (a) and vs the energy gap (b). (c) Relative anisotropy ($\Delta\tilde{g}$) for InSb quantum wells with an infinite barrier (black ■) and with a finite one (InSb/CdTe quantum wells, red ●) plotted vs the thickness of the quantum well. The numerical values of the data presented in these figures are provided in Ref. [65].

coming from remote bands and characterized by high **k** wave vectors that are not properly described in the envelope function approximation. Second, there are terms coming from chemical bonds and spin-orbit coupling which are specific to the surface atoms. Interestingly, our tight-binding calculations show that the total surface contribution is small or vanishing for the g-factor along a rotational axis of a nanostructure, in the strong confinement regime (Sec. VI and Appendix A). In that case, our tight-binding calculations show that the local orbital magnetic moment is weak close to the surface [see, for example, Figs. 6(a) and 6(b) for the spherical nanocrystal, and Fig. 7(a) for the circular nanoplatelet along z]. On the contrary, along axes characterized by a large g-factor anisotropy, the weight of the local orbital magnetic moment (of the spin-orbit induced circulating current) in the surface region is comparatively much higher [see Fig. 7(b) for the circular nanoplatelet along z]. However, more quantitative studies are required to understand the behavior of the surface terms.

VIII. CONCLUSIONS

In summary, we have calculated using a tight-binding approach the electron g-factors in strongly confined semiconductor nanostructures with various dimensionalities, sizes, and shapes, for several semiconductor compounds characterized by a direct gap at Γ. Electron g-factors are provided and analyzed for hundreds of configurations. For a given compound, a universal behavior is found versus the energy gap for all nanostructures. The g-factor for spherical nanocrystals is taken as a reference curve. For systems with a rotational symmetry axis, the g-factor along that axis is in excellent agreement with the reference curve. The g-factors along axes with broken rotational symmetry present more important deviations from the reference curve.

In order to explain this universal behavior, we have derived general expressions for the calculation of the magnetic moment and the g-tensor in nanostructures of arbitrary shape. We demonstrate that the g-tensor can be written as a sum of bulk and surface terms, the bulk term being the dominant one. Whatever the shape and dimensionality of the nanostructure, the bulk term is isotropic and is independent of the electron wave function, it just depends on the energy gap. The anisotropies are entirely due to the surface terms. Our expressions for the spin-orbit-induced orbital magnetic moment allow to interpret the results of the tight-binding calculations and to understand the physical origin of the universal behavior of g-factors. They also enable the prediction of the orbital magnetic moment density just from the knowledge of the electron envelope wave function.

ACKNOWLEDGMENT

The authors acknowledge fruitful discussions with Louis Biadala.

APPENDIX A: INFLUENCE OF A PASSIVATION SHELL ON THE g-FACTORS

In this appendix, we present a brief comparison between results obtained with infinite confining barriers and finite ones. We take InSb spherical nanocrystals as an example. For the infinite barrier case, we use the second passivation model (Sec. II A). For the finite barrier case, we consider a core-shell InSb/CdTe structure as described in Sec. II A (shell thickness = 1 nm). For this heterostructure, the barrier is finite but sufficiently large to remain in the strong confinement regime. The obtained g-factors are shown in Figs. 8(a) and 8(b). The two systems give similar results, and the effects of the finite barrier are quite small.

We also show in Fig. 8(c) the relative anisotropy ($\Delta\tilde{g}$) for InSb quantum wells, with finite or infinite barrier. Even if there are non-negligible discrepancies between the two sets of results, confirming the sensitivity of the anisotropies to the confining potential, the trends are very similar.

APPENDIX B: ORBITAL MAGNETIC MOMENT DENSITY IN A SPHERICAL NANOCRYSTAL AND IN A CIRCULAR NANOPLATELET

1. Spherical nanocrystal

We consider a magnetic field along z. For reasons of symmetry, we employ the cylindrical coordinates ρ (radial

distance), ϕ (azimuth angle), and z (height). The electron envelope wave function is given by Eq. (14) with $r = \sqrt{\rho^2 + z^2}$. The operator $x\frac{\partial}{\partial x} + y\frac{\partial}{\partial y}$ becomes $\rho\frac{\partial}{\partial \rho}$. We deduce from Eq. (16) the normalized density of orbital magnetic momentum (per unit cell volume)

$$\frac{V_0}{2\pi R}\frac{\rho^2}{r^2}\sin\left(\frac{\pi r}{R}\right)\left[\frac{1}{r^2}\sin\left(\frac{\pi r}{R}\right) - \frac{\pi}{Rr}\cos\left(\frac{\pi r}{R}\right)\right]. \quad \text{(B1)}$$

A 2D plot of this function is presented in Figs. 6(c) and 6(d).

2. Circular nanoplatelet

We consider a circular nanoplatelet of thickness L and radius R. The rotational symmetry axis is along z. The envelope wave function, solution of Eq. (9), is given in cylindrical coordinates by

$$F_s(\mathbf{r}) = \frac{1}{\sqrt{\pi}J_1(\alpha)R}\sqrt{\frac{2}{L}}J_0\left(\frac{\alpha\rho}{R}\right)\sin\left(\frac{\pi z}{L}\right), \quad \text{(B2)}$$

where J_0 and J_1 are Bessel functions of the first kind, and $\alpha \approx 2.4048$ is the first zero of J_0.

For a magnetic field along z, the normalized density of orbital magnetic momentum is given by

$$\frac{2V_0\alpha}{\pi L R^3 J_1^2(\alpha)}\rho J_0\left(\frac{\alpha\rho}{R}\right)J_1\left(\frac{\alpha\rho}{R}\right)\sin^2\left(\frac{\pi z}{L}\right). \quad \text{(B3)}$$

For a magnetic field along x, the solution becomes

$$-\frac{V_0}{L^2R^2J_1^2(\alpha)}zJ_0\left(\frac{\alpha\rho}{R}\right)\sin\left(\frac{2\pi z}{L}\right) + \frac{2V_0\alpha}{\pi L R^3 J_1^2(\alpha)}\frac{y^2}{\rho}J_0\left(\frac{\alpha\rho}{R}\right)J_1\left(\frac{\alpha\rho}{R}\right)\sin^2\left(\frac{\pi z}{L}\right). \quad \text{(B4)}$$

The 2D plots of these functions are presented in Figs. 7(c) and 7(d).

[1] D. Leonard, M. Krishnamurthy, C. M. Reaves, S. P. Denbaars, and P. M. Petroff, Appl. Phys. Lett. **63**, 3203 (1993).
[2] M. Skolnick and D. Mowbray, Annu. Rev. Mater. Res. **34**, 181 (2004).
[3] X. Hu, G. Li, and J. C. Yu, Langmuir **26**, 3031 (2010).
[4] D. V. Talapin, J.-S. Lee, M. V. Kovalenko, and E. V. Shevchenko, Chem. Rev. **110**, 389 (2010).
[5] M. D. Regulacio and M.-Y. Han, Acc. Chem. Res. **43**, 621 (2010).
[6] A. M. Smith and S. Nie, Acc. Chem. Res. **43**, 190 (2010).
[7] C. d. M. Donegá, Chem. Soc. Rev. **40**, 1512 (2011).
[8] S. Ithurria, M. D. Tessier, B. Mahler, R. P. S. M. Lobo, B. Dubertret, and A. L. Efros, Nat. Mater. **10**, 936 (2011).
[9] M. V. Kovalenko, L. Manna, A. Cabot, Z. Hens, D. V. Talapin, C. R. Kagan, V. I. Klimov, A. L. Rogach, P. Reiss, D. J. Milliron, P. Guyot-Sionnnest, G. Konstantatos, W. J. Parak, T. Hyeon, B. A. Korgel, C. B. Murray, and W. Heiss, ACS Nano **9**, 1012 (2015).
[10] D. Graham-Rowe, Nat. Photonics **3**, 307 (2009).
[11] S. E. Lohse and C. J. Murphy, J. Am. Chem. Soc. **134**, 15607 (2012).
[12] R. Freeman and I. Willner, Chem. Soc. Rev. **41**, 4067 (2012).
[13] P. V. Kamat, Acc. Chem. Res. **45**, 1906 (2012).
[14] G. H. Carey, A. L. Abdelhady, Z. Ning, S. M. Thon, O. M. Bakr, and E. H. Sargent, Chem. Rev. **115**, 12732 (2015).
[15] E. Lhuillier, M. Scarafagio, P. Hease, B. Nadal, H. Aubin, X. Z. Xu, N. Lequeux, G. Patriarche, S. Ithurria, and B. Dubertret, Nano Lett. **16**, 1282 (2016).
[16] R. Wang, Y. Shang, P. Kanjanaboos, W. Zhou, Z. Ning, and E. H. Sargent, Energy Environ. Sci. **9**, 1130 (2016).
[17] W. K. Liu, K. M. Whitaker, A. L. Smith, K. R. Kittilstved, B. H. Robinson, and D. R. Gamelin, Phys. Rev. Lett. **98**, 186804 (2007).
[18] L. Biadala, Y. Louyer, P. Tamarat, and B. Lounis, Phys. Rev. Lett. **105**, 157402 (2010).
[19] M. J. Fernée, C. Sinito, Y. Louyer, C. Potzner, T.-L. Nguyen, P. Mulvaney, P. Tamarat, and B. Lounis, Nat. Commun. **3**, 1287 (2012).
[20] F. Liu, L. Biadala, A. V. Rodina, D. R. Yakovlev, D. Dunker, C. Javaux, J.-P. Hermier, A. L. Efros, B. Dubertret, and M. Bayer, Phys. Rev. B **88**, 035302 (2013).
[21] Z. Zhang, Z. Jin, H. Ma, Y. Xu, X. Lin, G. Ma, and X. Sun, Phys. E **56**, 85 (2014).
[22] C. Sinito, M. J. Fernée, S. V. Goupalov, P. Mulvaney, P. Tamarat, and B. Lounis, ACS Nano **8**, 11651 (2014).
[23] A. Granados del Águila, B. Jha, F. Pietra, E. Groeneveld, C. de Mello Donegá, J. C. Maan, D. Vanmaekelbergh, and P. C. M. Christianen, ACS Nano **8**, 5921 (2014).
[24] M. Fujii, A. Mimura, S. Hayashi, Y. Yamamoto, and K. Murakami, Phys. Rev. Lett. **89**, 206805 (2002).
[25] D. J. Norris, A. L. Efros, and S. C. Erwin, Science **319**, 1776 (2008).
[26] R. N. Pereira, A. R. Stegner, T. Andlauer, K. Klein, H. Wiggers, M. S. Brandt, and M. Stutzmann, Phys. Rev. B **79**, 161304 (2009).
[27] A. M. Schimpf, K. E. Knowles, G. M. Carroll, and D. R. Gamelin, Acc. Chem. Res. **48**, 1929 (2015).
[28] J. Jeong, B. Yoon, Y.-W. Kwon, D. Choi, and K. S. Jeong, Nano Lett. **17**, 1187 (2017).
[29] E. Lifshitz, L. Fradkin, A. Glozman, and L. Langof, Annu. Rev. Phys. Chem. **55**, 509 (2004).
[30] D. Loss and D. P. DiVincenzo, Phys. Rev. A **57**, 120 (1998).
[31] S. Nadj-Perge, S. M. Frolov, E. P. A. M. Bakkers, and L. P. Kouwenhoven, Nature (London) **468**, 1084 (2010).
[32] R. J. Warburton, Nat. Mater. **12**, 483 (2013).
[33] G. Cao, H.-O. Li, G.-D. Yu, B.-C. Wang, B.-B. Chen, X.-X. Song, M. Xiao, G.-C. Guo, H.-W. Jiang, X. Hu, and G.-P. Guo, Phys. Rev. Lett. **116**, 086801 (2016).
[34] E. Ivchenko, A. Kiselev, and M. Willander, Solid State Commun. **102**, 375 (1997).
[35] E. I. Rashba and A. L. Efros, Phys. Rev. Lett. **91**, 126405 (2003).
[36] Y. Kato, R. C. Myers, D. C. Driscoll, A. C. Gossard, J. Levy, and D. D. Awschalom, Science **299**, 1201 (2003).

[37] F. Klotz, V. Jovanov, J. Kierig, E. C. Clark, D. Rudolph, D. Heiss, M. Bichler, G. Abstreiter, M. S. Brandt, and J. J. Finley, Appl. Phys. Lett. **96**, 053113 (2010).

[38] M. W. Taylor, P. Spencer, E. Clarke, E. Harbord, and R. Murray, J. Phys. D: Appl. Phys. **46**, 505105 (2013).

[39] A. L. Efros, M. Rosen, M. Kuno, M. Nirmal, D. J. Norris, and M. Bawendi, Phys. Rev. B **54**, 4843 (1996).

[40] A. A. Kiselev, E. L. Ivchenko, and U. Rössler, Phys. Rev. B **58**, 16353 (1998).

[41] R. Winkler, *Spin-Orbit Coupling Effects in Two-Dimensional Electron and Hole Systems*, Springer Tracts in Modern Physics Vol. 191 (Springer-Verlag, Berlin, Heidelberg, New York, 2003).

[42] A. V. Rodina, A. L. Efros, and A. Y. Alekseev, Phys. Rev. B **67**, 155312 (2003).

[43] J. Schrier and K. B. Whaley, Phys. Rev. B **67**, 235301 (2003).

[44] E. L. Ivchenko, Phys. Usp. **55**, 808 (2012).

[45] J. A. Gupta, D. D. Awschalom, A. L. Efros, and A. V. Rodina, Phys. Rev. B **66**, 125307 (2002).

[46] J. M. Luttinger and W. Kohn, Phys. Rev. **97**, 869 (1955).

[47] E. O. Kane, J. Phys. Chem. Sol. **1**, 249 (1957).

[48] I. A. Yugova, A. Greilich, D. R. Yakovlev, A. A. Kiselev, M. Bayer, V. V. Petrov, Y. K. Dolgikh, D. Reuter, and A. D. Wieck, Phys. Rev. B **75**, 245302 (2007).

[49] J. van Bree, A. Y. Silov, P. M. Koenraad, and M. E. Flatté, Phys. Rev. Lett. **112**, 187201 (2014).

[50] J. van Bree, A. Y. Silov, M. L. van Maasakkers, C. E. Pryor, M. E. Flatté, and P. M. Koenraad, Phys. Rev. B **93**, 035311 (2016).

[51] E. Kalesaki, C. Delerue, C. Morais Smith, W. Beugeling, G. Allan, and D. Vanmaekelbergh, Phys. Rev. X **4**, 011010 (2014).

[52] E. Kalesaki, W. H. Evers, G. Allan, D. Vanmaekelbergh, and C. Delerue, Phys. Rev. B **88**, 115431 (2013).

[53] J.-M. Jancu, R. Scholz, F. Beltram, and F. Bassani, Phys. Rev. B **57**, 6493 (1998).

[54] A. Tadjine, G. Allan, and C. Delerue, Phys. Rev. B **94**, 075441 (2016).

[55] J. C. Slater and G. F. Koster, Phys. Rev. **94**, 1498 (1954).

[56] G. Bastard, *Wave Mechanics Applied to Semiconductor Heterostructures*, Monographies de Physique (Les Éditions de Physique, Les Ulis, 1988).

[57] C. Delerue and M. Lannoo, *Nanostructures: Theory and Modeling* (Springer, Berlin, 2004).

[58] Y. Hinuma, A. Grüneis, G. Kresse, and F. Oba, Phys. Rev. B **90**, 155405 (2014).

[59] M. Graf and P. Vogl, Phys. Rev. B **51**, 4940 (1995).

[60] Y. M. Niquet, C. Delerue, G. Allan, and M. Lannoo, Phys. Rev. B **62**, 5109 (2000).

[61] In principle, one should diagonalize the 2×2 matrix of the perturbation Hamiltonian written in the basis of spin up and down states which are degenerate. However, we have checked that the error made by using Eq. (1) instead of this approach is below 3% in all cases.

[62] H. Van Vleck, *The Theory of Electric and Magnetic Susceptibilities* (Oxford, New York, 1932).

[63] L. M. Roth, B. Lax, and S. Zwerdling, Phys. Rev. **114**, 90 (1959).

[64] J.-M. Jancu, R. Scholz, E. A. de Andrada e Silva, and G. C. La Rocca, Phys. Rev. B **72**, 193201 (2005).

[65] See Supplemental Material at http://link.aps.org/supplemental/10.1103/PhysRevB.95.235437 for the numerical values of all data presented in the figures of the main document, for additional results including comparisons with experiments, and for tests of convergence of g-factor calculations.

[66] W. W. Piper, in *Proceedings of the 7th International Conference on II-VI Semiconductors Compounds*, edited by D. G. Thomas (Benjamin, New York, 1967), p. 839.

[67] O. Gywat, H. J. Krenner, and J. Berezovsky, *Spins in Optically Active Quantum Dots: Concepts and Methods* (Wiley-VCH Verlag, Weinheim, 2009).

[68] M. Oestreich, S. Hallstein, A. P. Heberle, K. Eberl, E. Bauser, and W. W. Rühle, Phys. Rev. B **53**, 7911 (1996).

[69] P. Pfeffer and W. Zawadzki, J. Appl. Phys. **111**, 083705 (2012).

[70] C. Weisbuch and C. Hermann, Phys. Rev. B **15**, 816 (1977).

[71] I. Vurgaftman, J. R. Meyer, and L. R. Ram-Mohan, J. Appl. Phys. **89**, 5815 (2001).

[72] J. Konopka, Phys. Lett. A **26**, 29 (1967).

[73] G. Bemski, Phys. Rev. Lett. **4**, 62 (1960).

[74] R. A. Isaacson, Phys. Rev. **169**, 312 (1968).

[75] M. H. L. Pryce, Proc. Phys. Soc. Sec. A **63**, 25 (1950).

[76] I. van Weperen, S. R. Plissard, E. P. A. M. Bakkers, S. M. Frolov, and L. P. Kouwenhoven, Nano Lett. **13**, 387 (2013).

[77] Y. Tan, M. Povolotskyi, T. Kubis, Y. He, Z. Jiang, G. Klimeck, and T. B. Boykin, J. Comput. Electron. **12**, 56 (2013).

[78] R. Benchamekh, F. Raouafi, J. Even, F. Ben Cheikh Larbi, P. Voisin, and J.-M. Jancu, Phys. Rev. B **91**, 045118 (2015).

[79] C. E. Pryor and M. E. Flatté, Phys. Rev. Lett. **96**, 026804 (2006).

[80] B. J. Witek, R. W. Heeres, U. Perinetti, E. P. A. M. Bakkers, L. P. Kouwenhoven, and V. Zwiller, Phys. Rev. B **84**, 195305 (2011).

[81] M. Kuwahara, T. Kutsuwa, K. Ono, and H. Kosaka, Appl. Phys. Lett. **96**, 163107 (2010).

[82] A. A. Sirenko, T. Ruf, M. Cardona, D. R. Yakovlev, W. Ossau, A. Waag, and G. Landwehr, Phys. Rev. B **56**, 2114 (1997).

[83] M. Syperek, D. R. Yakovlev, I. A. Yugova, J. Misiewicz, M. Jetter, M. Schulz, P. Michler, and M. Bayer, Phys. Rev. B **86**, 125320 (2012).

[84] A. A. Sirenko, T. Ruf, A. Kurtenbachand, and K. Eberl, in *Proceedings of the 23rd International Conference on the Physics of Semiconductors*, edited by M. Scheffler and R. Zimmermann (World Scientific, Singapore, 1996), p. 1385.

[85] Y. Masumoto, I. V. Ignatiev, K. Nishibayashi, T. Okuno, S. Y. Verbin, and I. A. Yugova, J. Lumin. **108**, 177 (2004).

[86] Y. Masumoto, K. Kawana, and S. Tomimoto, Physica E: Low. Dimens. Syst. Nanostruct. **42**, 2493 (2010).

[87] J. Skiba-Szymanska, E. A. Chekhovich, A. V. Nikolaenko, A. I. Tartakovskii, M. N. Makhonin, I. Drouzas, M. S. Skolnick, and A. B. Krysa, Phys. Rev. B **77**, 165338 (2008).

[88] Y.-M. Niquet and D. C. Mojica, Phys. Rev. B **77**, 115316 (2008).

[89] C. Pryor, M.-E. Pistol, and L. Samuelson, Phys. Rev. B **56**, 10404 (1997).

[90] C. Bouet, M. D. Tessier, S. Ithurria, B. Mahler, B. Nadal, and B. Dubertret, Chem. Mater. **25**, 1262 (2013).

[91] M. G. Lopez, D. Vanderbilt, T. Thonhauser, and I. Souza, Phys. Rev. B **85**, 014435 (2012).

[92] G. Koster, J. O. Dimmock, R. G. Wheeler, and H. Statz, *Properties of the Thirty-Two Point Groups*, Massachusetts Institute of Technology Press Research Monograph (M.I.T. Press, Cambridge, 1963).

[93] M. Cardona and F. H. Pollak, Phys. Rev. **142**, 530 (1966).

[94] S. Richard, F. Aniel, and G. Fishman, Phys. Rev. B **70**, 235204 (2004).

[95] P. Löwdin, J. Math. Phys. **3**, 969 (1962).